

PAPER • **OPEN ACCESS**

Modeling resistive-inductive evolution of currents in Wendelstein 7-X













To cite this article: L. van Ham *et al* 2025 *Nucl. Fusion* **65** 036001

View the [article online](#) for updates and enhancements.

You may also like

- [Power loss by resonance radiation from a dc neon glow discharge at low pressures and low currents](#)
St Franke, H Deutsch, A Dinklage et al.
- [Resonant influence of helicity on Alfvén heating of plasma in stellarators](#)
I O Girka, V I Lapshin and R Schneider
- [The effects of non-uniform drive on plasma filaments](#)
Brendan Shanahan, Ben Dudson and Peter Hill

Modeling resistive-inductive evolution of currents in Wendelstein 7-X

L. van Ham^{1,*} , S.A. Lazerson² , J.C. Schmitt³ , B.F. Lee⁴ , M. Beurskens^{1,a} , K.J. Brunner¹ , N. Chaudhary¹ , G. Fuchert¹, J. Geiger¹ , M. Hirsch¹, J. Knauer¹, A. Langenberg¹ , J.W. Oosterbeek¹, N. Pablant⁴ , E. Pasch¹, K. Rahbarnia¹ , G. Weir¹  and the W7-X Team^{1,b}

¹ Max-Planck-Institut für Plasmaphysik, 17491 Greifswald, Germany

² Gauss Fusion GmbH, 85748 Garching bei München, Germany

³ Auburn University, Auburn, AL, United States of America

⁴ Princeton University Plasma Physics Laboratory, Princeton, NJ, United States of America

E-mail: lucas.van.ham@ipp.mpg.de

Received 13 December 2024, revised 20 January 2025

Accepted for publication 27 January 2025

Published 7 February 2025



Abstract

This research investigates the temporal evolution of the toroidal plasma current in the Wendelstein 7-X (W7-X) stellarator under different heating, fueling, and current drive scenarios. The THRIFT code has been modernized and its predictions of the evolution of the toroidal current have been compared against experimentally measured currents in W7-X. Good agreement is found with respect to the characteristic timescale between experimentally measured and simulated toroidal currents. The total bootstrap current is under-predicted owing to the applicability of the BOOTSJ model for the plasma collisionalities in question. Edge plasma resistivity is found to play an important role in the asymptotic behavior of the evolution of the current, indicating a possible limitation of the minimum plasma temperature when applying this model. Simulations of ECCD and heating power steps show THRIFT is capable of capturing the dynamical evolution of the current in response to changes in current sources. Future uses of THRIFT include validating and benchmarking other non-inductive current models.

Keywords: Wendelstein 7-X, bootstrap current, current drive, THRIFT, BOOTSJ

(Some figures may appear in colour only in the online journal)

1. Introduction

Wendelstein 7-X (W7-X) is a five-field period, low-shear superconducting stellarator of the Helias type operating in

Greifswald, Germany. It has been optimized according to a set of criteria, including good magnetohydrodynamic (MHD) stability, small bootstrap currents, and low neoclassical transport [1]. It can generate a variety of magnetic configurations, including different rotational transform profiles and mirror ratios, made possible by its 50 non-planar coils and 20 planar superconducting coils [2]. The main purpose of W7-X is to demonstrate the viability of optimized stellarators as fusion power plants [3].

Instrumental in achieving this goal is the performance of its island divertor, which relies on the presence of magnetic islands appearing on the plasma edge when the rotational transform ι satisfies $\iota = 5/m$, with m an integer [4]. Changes in the edge rotational transform ι_a or its shear will modify the

^a Dr. Marc Beurskens passed away on 11 April 2024.

^b See Grulke *et al* 2024 (<https://doi.org/10.1088/1741-4326/ad2f4d>) for the W7-X Team.

* Author to whom any correspondence should be addressed.



Original Content from this work may be used under the terms of the [Creative Commons Attribution 4.0 licence](https://creativecommons.org/licenses/by/4.0/). Any further distribution of this work must maintain attribution to the author(s) and the title of the work, journal citation and DOI.

position or size of these islands, causing the patterns of particle deposition and power on the divertor targets to change [5, 6]. The rotational transform depends on the magnitude of the total toroidal current [7]. Therefore, to control the edge rotational transform and maintain good divertor operation, a good understanding of the behavior of the total toroidal current for different W7-X scenarios is required [8].

An important driver of the total toroidal current in W7-X is the bootstrap current, which is a current driven by temperature and density gradients and arises from collisions between passing and trapped particles [9]. The bootstrap current depends non-trivially on the plasma collisionality, radial electric field, and magnetic field configuration [10]. Bootstrap currents greater than 20 kA can be present in W7-X plasmas [11]. Several models for estimating the bootstrap current to varying degrees of accuracy exist (e.g. SFINCS [12], DKES [13, 14], NEOTRANSF [15–17], BOOTSJ [18–20]). Toroidal currents can also be driven through external means, such as through RF heating (Electron Cyclotron Current Drive (ECCD), Ion Cyclotron Current Drive (ICCD)) or neutral beam injection (Neutral Beam Current Drive (NBCD)). All current sources (bootstrap current and externally driven currents) must be considered to evaluate the total toroidal current, and validated numerical models of each of these current sources are therefore necessary.

Validation of such models for W7-X is hindered by the non-trivial time-evolution of the total toroidal current. Modeling the plasma as a simple LR-circuit, the total toroidal current I can be shown to evolve as (assuming stationary plasma profiles)

$$I(t) = I_{\infty} (1 - \exp(-t/\tau_{L/R})) , \quad (1)$$

where

$$I_{\infty} = I_{\text{boot}} + I_{\text{CD}} = \text{steady state toroidal current}, \\ \tau = L/R = L/R - \text{time or resistive} - \text{inductive time}.$$

Due to the long L/R -time in W7-X, the total toroidal current does not typically saturate before the end of a discharge [21] and I_{∞} must be obtained from curve-fitting equation (1). This procedure is accompanied by a degree of uncertainty as plasma conditions are never exactly stationary. Compounding this uncertainty is that as the total toroidal current evolves, the magnetic field evolves with it, in turn modifying the source currents. For self-consistent results, the effect of the total toroidal current on the magnetic field must be considered. This step is often omitted as it is assumed that this effect is small [22]. For example, NTSS [15] calculations of the bootstrap current for different W7-X configurations and plasma conditions [10, 23] did not take this effect into account. No investigation into the evolution of the total toroidal current with self-consistent magnetic field and bootstrap currents for W7-X has been performed as of yet.

In this paper, we investigate the evolution of the total toroidal current in W7-X with self-consistent magnetic field and bootstrap current. The THRIFT code [7, 24], which models the evolution of the total toroidal current, is re-implemented. This implementation is parallelized, dynamically coupled to VMEC [25] to update the magnetic equilibrium, and uses the STELLOPT code suite [26]. The implementation is described and benchmarked in section 2. THRIFT simulations of the total toroidal current are compared against experimentally measured toroidal currents in W7-X for a few discharges to gauge the accuracy of BOOTSJ in section 3. This section includes ECCD scenarios in W7-X simulated using THRIFT. We discuss the results of this investigation in section 4.

2. The THRIFT code

The THRIFT code models the evolution of toroidal currents in plasmas with general three-dimensional magnetic configurations. It assumes that the magnetic flux surfaces form nested tori, in which case the evolution of the total toroidal current is described by a one-dimensional diffusion equation for the rotational transform, given by [7]

$$\frac{d\iota}{dt} = \frac{d\iota}{d\Phi} \frac{d\Phi}{dt} + \frac{d}{d\Phi} \left(\frac{\eta_{\parallel}}{\mu_0} \Phi' (S_{11}\iota + S_{12})^2 \frac{d}{dr} \left(\frac{S_{11}\iota + S_{12}}{S_{21}\iota + S_{22}} \right) - \eta_{\parallel} \langle J_{\text{source}} B \rangle \frac{dV}{d\Phi} \right), \quad (2)$$

where

$$\begin{aligned} \Phi &= \text{toroidal magnetic flux}, \\ \eta_{\parallel} &= \text{parallel electrical resistivity}, \\ S_{ij} &= \text{susceptance matrix elements [7]}, \\ J_{\text{source}} &= \text{source current density}, \\ B &= \text{magnetic field strength}, \\ V &= \text{plasma volume}. \end{aligned}$$

The prime denotes a derivative with respect to the radial variable r . Only the resistive-inductive behavior of the plasma is modeled. The effect of magnetic islands, which cause particles (and hence currents) to be redistributed on timescales shorter than the resistive-inductive time, is not captured. A novel implementation of this equation for easier interfacing with more recent codes is discussed.

2.1. Implementation details

The flux surface label $s = \Phi/\Phi_a$ was chosen (as opposed to $\rho = (\Phi/\Phi_a)^{1/2}$) as the basis of the spatial grid to avoid $1/\rho$ singularities near the magnetic axis and to simplify conversion between toroidal current densities and toroidal currents. Introducing additional relationships between pressure

and currents [27] and neglecting the term proportional to $d\Phi/dt$ [7], equation (2) may be written as [28]

$$S_{11} \frac{d\iota}{dt} = \frac{S_{11}}{\Phi_a^2} \frac{d}{ds} \left(\eta_{\parallel} V' \left(\frac{\langle B^2 \rangle}{\mu_0} \frac{d}{ds} (S_{11}\iota + S_{12}) + p' (S_{11}\iota + S_{12}) - \langle J_{\text{source}} B \rangle \right) \right), \quad (3)$$

where p is the plasma pressure. Equation (3) was discretized using a backwards time, centered space (BTCS) scheme. The boundary condition at the plasma center is taken to be absence of a net toroidal current, i.e.

$$I(s=0, t) = 0. \quad (4)$$

Note that this does not necessarily imply that the total toroidal current *density* is zero at the plasma center. The boundary condition at the plasma edge was taken to be [29]

$$E_{\parallel}(s=1, t) = -\frac{L_{\text{ext}}}{2\pi R} \frac{dI}{dt} \Big|_{s=1}, \quad (5)$$

where

$$\begin{aligned} E_{\parallel} &= \text{parallel electric field,} \\ L_{\text{ext}} &\approx \mu_0 R (\ln(8R/a) - 2) \\ &= \text{plasma external inductance,} \\ R &= \text{plasma major radius,} \\ a &= \text{plasma minor radius.} \end{aligned}$$

We note that elsewhere in the plasma, we may determine the parallel electric field using $E_{\parallel} = \eta_{\parallel} J_{\text{shield}}$, where $J_{\text{shield}} = J - J_{\text{source}}$ is the shielding current density. The time-derivative of the total toroidal current in equation (5) was approximated using a backwards Euler scheme. A second-order accurate expression for the edge parallel electric field was used.

As an initial condition, THRIFT assumes that no currents are in the plasma upon start-up, i.e.

$$I(s, t=0) = 0. \quad (6)$$

The parameters related to the magnetic field may be obtained from a suitable magnetic equilibrium code. VMEC [25] was selected to fulfill this purpose as it shares the assumption of nested toroidal flux surfaces with THRIFT.

In this work, η_{\parallel} was estimated using the model by Sauter *et al* [30]. While this approach allows for a rapid calculation of the resistivity, the model was specifically derived for axisymmetric equilibria and may therefore not be valid when applied to non-axisymmetric systems such as W7-X. Nevertheless, it is considered as a good starting point for our implementation and can be replaced with more accurate numerical models in future applications.

The workflow of THRIFT to evolve the total toroidal current for a given scenario is as follows. Each scenario is first discretized into nt time iterations. For each time iteration n , the plasma profiles are read from an input HDF5 file. Inside

a Picard loop with index k , the magnetic field is first calculated using VMEC, after which the resistivity and any source currents are determined using the appropriate methods. The system of equations (3)–(6) is then solved to obtain a first-stage estimate of the total toroidal current density $\{J\}_k^n$. The second-stage estimate $\{J\}_k^n$ is determined from its value at the previous Picard iteration $\{J\}_{k-1}^n$ (or at the previous time iteration $\{J\}^{n-1}$ if $k=1$) and a Picard factor $f=0.75$, using

$$\{J\}_k^n = (1-f) \{J\}_{k-1}^n + f \{\hat{J}\}_k^n. \quad (7)$$

The Picard factor is used to help with numerical convergence. Self-consistency between the magnetic field, source currents, and total toroidal current is achieved by repeating this procedure until the relative change in $\{J\}_k^n$ between two Picard iterations,

$$\{\Delta J\}_k^n = \left| \frac{\{J\}_k^n - \{J\}_{k-1}^n}{\{J\}_{k-1}^n} \right| \quad (8)$$

is smaller than a threshold value $\Delta_{\text{tol}} = 0.01$ on the full spatial grid. Alternatively, the Picard loop may be terminated before convergence is reached if the maximum number of Picard iterations is exceeded. A diagram of this iteration scheme is shown in figure 1.

2.2. Verification

The evolution of the parallel electric field (and hence the total toroidal current) is exactly known for the case of a circular cross-section, large aspect-ratio tokamak with a temporally invariant, spatially uniform resistivity profile and a temporally invariant source current profile [29]. Under these conditions, the parallel electric field can be written as a Fourier–Bessel (FB) series, given by

$$E^{\text{FB}}(x, t) = \sum_{n=1}^{\infty} f_n F_n(x) \exp(-t/\tau_n), \quad (9)$$

where

$$\begin{aligned} \tau_n &= \mu_0 \sigma_0 a^2 / k_n^2, \\ &= \text{mode decay time,} \\ f_n &= \text{mode amplitude,} \\ F_n(x) &= \tilde{J}_0(k_n x), \\ \sigma_0 &= \text{core electrical conductivity.} \end{aligned}$$

The \tilde{J}_i are Bessel functions of the first kind and $k_n > 0$ is the n th root of

$$\tilde{J}_0(k) - I_{\text{ext}}^* k \tilde{J}_1(k) = 0, \quad (10)$$

where $I_{\text{ext}}^* = L_{\text{ext}}/(\mu_0 R)$ and $\tilde{J}_1(k) = \tilde{J}'_0(k)$.

This scenario was recreated to verify the numerical implementation of THRIFT. A VMEC equilibrium was generated for a circular-cross-section, large-aspect-ratio hypothetical

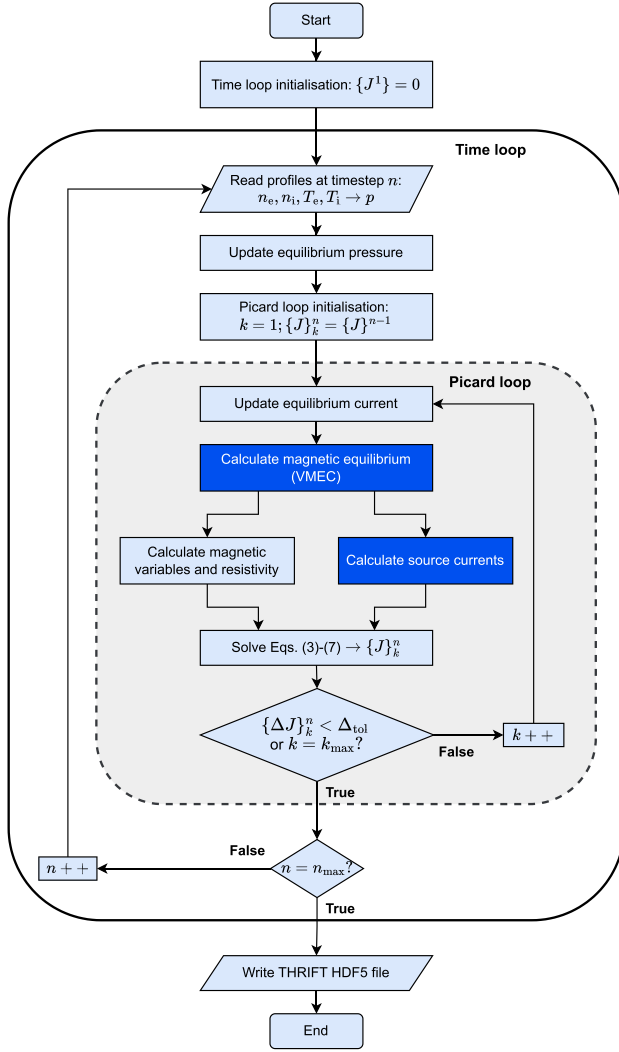


Figure 1. Flowchart of the THRIFT method. Dark blue shapes indicate when external codes are (or could be) called, light blue shapes indicate processes performed by THRIFT routines.

tokamak with $R = 1000\text{ m}$, $a = 1\text{ m}$, $B_0 = 4\text{ T}$ to match the conditions mentioned above. Plasma density and temperature profiles used were $T_e = 100\text{ eV}$, $n_e = n_i = 5 \cdot 10^{19}\text{ m}^{-3}$, $T_i(\rho) = (1 - 2\rho + \rho^2)\text{ keV}$. These profiles were chosen to ensure that the resistivity profile would be spatially uniform and p' would be finite. Since equation (6) enforces zero net toroidal current at the start of the simulation, the rotational transform is initially zero everywhere and a pressure gradient cannot be sustained, causing VMEC to not converge to a solution. To avoid this issue, the density and temperature profiles were asymptotically scaled towards the given values over approximately 3 s. A toy bootstrap current model was used, given by [31]

$$J_{\text{boot}}(s) = \frac{\sqrt{\epsilon}R}{\Phi_a} sp'(s). \quad (11)$$

where ϵ is the inverse aspect ratio. The scenario was simulated using THRIFT for a duration of 50 s. The coefficients f_n and decay times τ_n were determined from the simulated electric

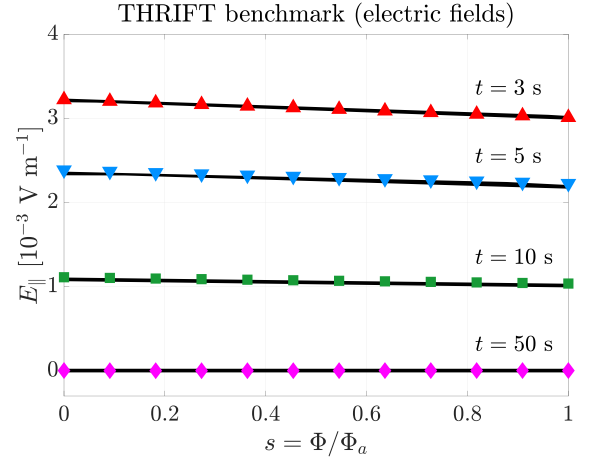


Figure 2. THRIFT (lines) and Fourier–Bessel (shapes) parallel electric field for the tokamak benchmark case.

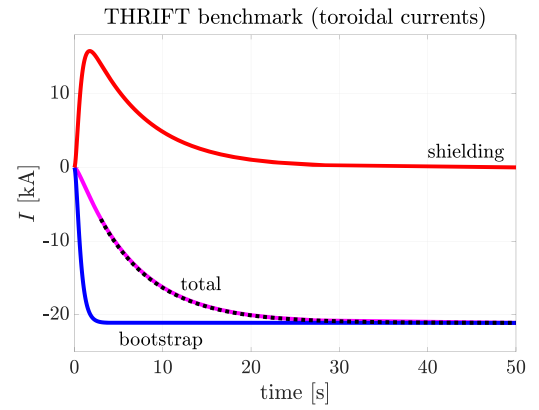


Figure 3. Toroidal current make-up for the tokamak benchmark case. The dotted line indicates the Fourier–Bessel estimate of the total current.

field at $t = 3\text{ s}$, after which the predicted electric field was calculated from equation (9).

Figure 2 depicts the THRIFT (lines) and the FB (shapes) electric field at selected snapshots of the simulation. The two quantities are in good agreement with each other and both decay towards zero in steady-state. The toroidal currents for this case are shown in figure 3. The THRIFT current and FB current are again in good agreement with each other and both asymptotically evolve towards the bootstrap current. The estimated decay times for the currents are $\tau_{L/R} = 6.54\text{ s}$ (THRIFT) and $\tau_{L/R} = 6.48\text{ s}$ (FB). The small disagreement between the FB and THRIFT electric field is mainly attributed to the temperature and density profiles not having completely stabilized by $t = 3\text{ s}$. The bootstrap current and resistivity varied as a result by about 0.5% and 0.4%, respectively. The convergence tolerance THRIFT used for the current density is also on the same order as the disagreement and has possibly also contributed to the error. Overall, the results show that the numerical implementation has been successful and verify the functioning of THRIFT.

3. Current evolution simulations for W7-X

THRIFT is used to self-consistently simulate the evolution of the total toroidal current for a few different scenarios in W7-X. Experiments of interest are those in which the measured toroidal current evolves asymptotically, which can be curve-fit with equation (1) to obtain I_∞ and $\tau_{L/R}$. The same approach can be applied to results from THRIFT. If no current drive is present, I_∞ corresponds to the bootstrap current. This approach allows for validation of THRIFT for W7-X as well as investigating the accuracy of the numerical model used to estimate the bootstrap current for these cases.

This work employs BOOTSJ, which calculates the bootstrap current using a semi-analytical model in the limit of a long mean-free-path, large aspect ratio, collisionless plasma [18–20]. Previous publications have claimed that its results are still accurate for W7-X [32], HSX [33], and a spherical tokamak with 3D effects [34]. However, in a more recent publication, BOOTSJ is benchmarked against SFINCS for a quasi-axisymmetric design and performed poorly [35]. Further investigation into the applicability of BOOTSJ to W7-X discharges is therefore of interest.

Additionally, BOOTSJ is one of only a few numerically tractable codes which can rapidly calculate bootstrap currents. It is thus suitable for interfacing with THRIFT, where the bootstrap current needs to be calculated many times in a single discharge. Recently, a similarly fast code named MONKES [36] has been developed which may be considered in the future.

3.1. THRIFT validation

Three experimental discharges, representative of operations at W7-X, were selected to be simulated. Discharge 20 180 828.30 (Case I, figure 4) is a low-iota ($\iota_a = 5/6$) discharge featuring a constant 2.5 MW ECRH power during 20 s of operation. Plasma conditions (density and temperature) are stable. The toroidal current evolves asymptotically and reaches 13 kA before the experiment is terminated.

Discharge 20 180 906.13 (Case II, figure 5) is a standard-iota ($\iota_a = 5/5$) discharge featuring a constant 4 MW ECRH power over 14 s of operation. Plasma conditions for this discharge are also stable. The toroidal current also evolves asymptotically and reaches 7 kA before the experiment is terminated.

Finally, discharge 20 181 004.45 (Case III, figure 6) is a reversed-field, low-iota discharge. It features 5 MW of ECRH power for a duration of 8 s, after which it is stepped down to 3 MW for the remaining 4 s of the experiment. The plasma parameters are relatively stable between $t \approx 0.5$ s and $t \approx 3.3$ s. Between $t \approx 3.3$ s and $t \approx 8$ s, plasma density increases and temperature decreases. After the power step-down, the plasma density is stable whereas plasma temperatures drop sharply. The toroidal current is continuously increasing prior to the heating step-down and decreases after ECRH power is reduced. This case is expected to exhibit a significant change in source currents after the heating step and it allows us to investigate how such changes affect the THRIFT prediction.

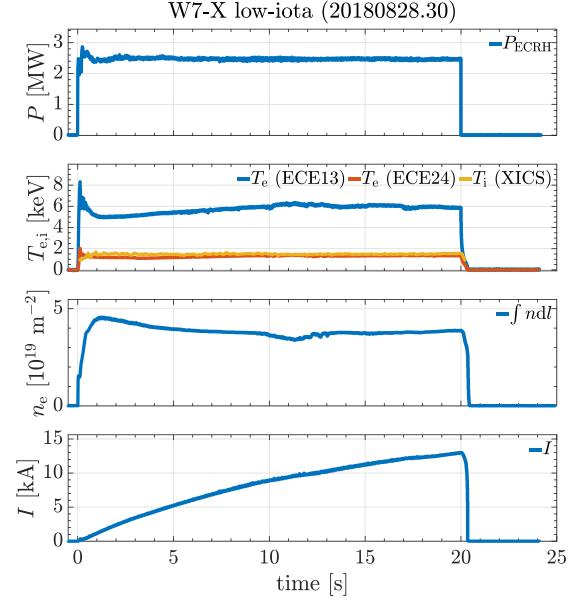


Figure 4. Overview of measured quantities in case I. From top to bottom: ECRH power, temperature, line-integrated density, diamagnetic energy, toroidal current. Electron temperatures are measured at the plasma core (ECE13) and approximately at the mid-radius (ECE24).

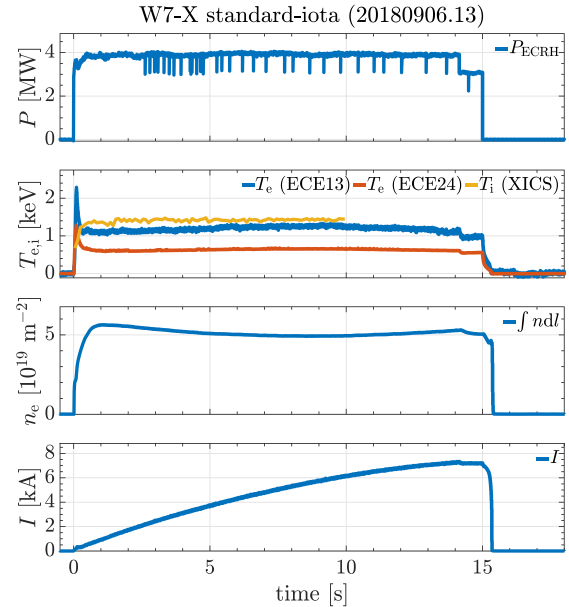


Figure 5. Overview of measured quantities in case II.

Each of these discharges used two ECRH launchers depositing power in stellarator-symmetric fashion to cancel out any residual RF current drive. Both launchers had mirror angles and sources selected in a manner that was believed to minimize the current drive. The exact amount of current driven by ECRH heating under these conditions was not known but was anticipated to be negligible compared to the bootstrap currents observed in these cases.

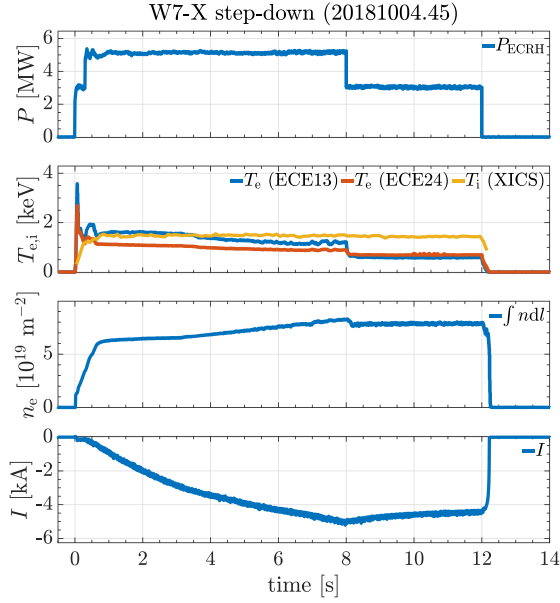


Figure 6. Overview of measured quantities in case III.

Thompson scattering was used to measure electron temperatures and densities. Ion temperatures were measured using x-ray Imaging Crystal Spectroscopy (XICS). Experimental measurements of these parameters were converted into usable profiles using WAPID_FIT [37]. The resulting profiles were then interpolated on the spatial grid using cubic Hermite splines. This last procedure included enforcing the edge boundary condition

$$T_{e,i} = 0 \text{ eV}, \quad (12)$$

which causes the electrical resistivity to diverge in the plasma edge ($\eta_{\parallel} \propto T_e^{-3/2}$). To mitigate this issue, temperatures were not allowed to drop below 14 eV, corresponding to the ionization temperature of hydrogen. The plasma was assumed to consist purely of hydrogen ($Z_{\text{eff}} = 1$) and quasi-neutrality was achieved by enforcing $n_i = n_e$ in the plasma. The density and temperature profiles had uncertainties of about $\pm 5\%$. Finally, BOOTSJ was initialized with $m = 32$ poloidal Boozer modes, $n = 16$ toroidal Boozer modes, and a damping factor of $\Delta_{\text{damp}} = 0.1$.

3.1.1. Fixed heating. Figures 7 and 8 show the evolution of the total toroidal current in experiment (red) and as calculated by THRIFT (magenta) for case I and case II, respectively. The values of $\tau_{L/R}$ and I_{∞} obtained from experiment and THRIFT as well as I_{boot} from BOOTSJ are shown in table 1.

The simulated total toroidal currents evolve asymptotically just as the experimental currents. The decay times of both toroidal currents are in agreement with each other, differing by 3.6% for case I and by 8.8% for case II. This agreement indicates that THRIFT is accurately capturing the time-behavior of the total toroidal current in these cases. The magnitudes of the simulated total toroidal currents disagree with experimental observations. The simulation I_{∞} is smaller than the

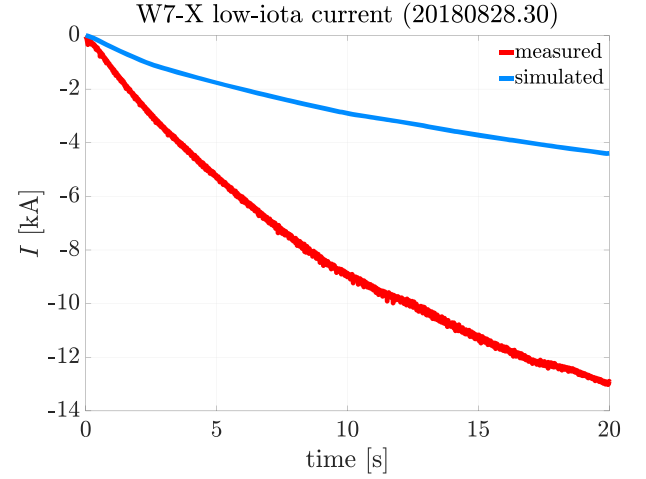


Figure 7. Comparison of simulated and measured currents for case I.

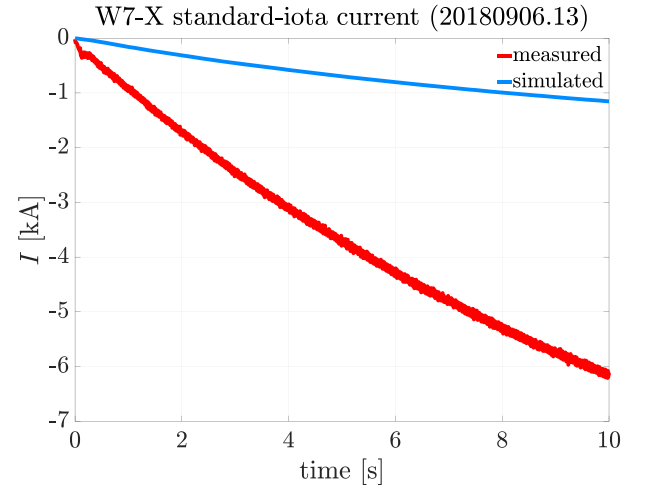


Figure 8. Comparison of simulated and measured currents for case II.

experimental I_{∞} by about 66% for case I and about 82% for case II. Furthermore, the extrapolated steady-state current for simulations disagrees with the bootstrap current calculated by BOOTSJ.

The latter issue is explained by the behavior of the parallel electric field, shown in figure 9. Here, the simulation was artificially extended to $t = 80$ s by keeping the profiles unchanged after $t = 19.6$ s to allow the total toroidal current to saturate. The edge electric field nearly vanishes at $t = 80$ s as dictated by the edge boundary condition, but the strong edge peaking causes an electric field to be ‘frozen-in’ inside the plasma, leading to a finite shielding current in the plasma even in steady-state. This peaking is nonphysical and occurs because the magnitude of the resistivity strongly grows in the plasma edge despite the temperature clamp. This issue can be mitigated by imposing a more aggressive temperature clamp (estimated at $T \approx 100$ eV) or by using a different model for the resistivity.

Table 1. Summary of results. Decay times $\tau_{L/R}$ and steady-state currents I_∞ were obtained from curve fitting. Uncertainties indicate goodness of fits. The mean bootstrap current I_{BS} at mid-radius is also indicated.

	$\tau_{L/R}$ [s]		I_∞ [kA]		I_{BS} [kA]
	measured	simulated	measured	simulated	
Case I	12.76 ± 0.36	13.22 ± 0.002	16.32 ± 0.24	5.53 ± 0.03	8.65
Case II	12.16 ± 0.07	11.09 ± 0.003	10.59 ± 0.002	1.91 ± 0.001	3.31

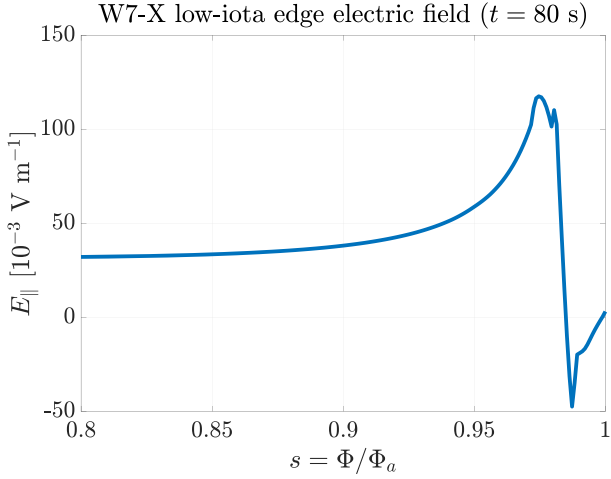


Figure 9. Evolution of parallel electric field in the plasma edge for case I.

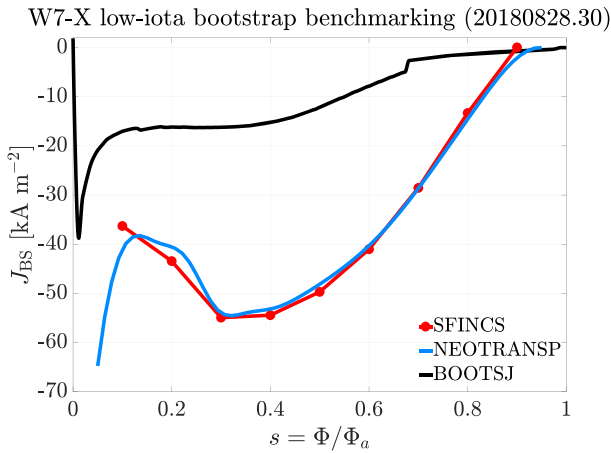


Figure 10. Bootstrap current density as calculated by three different codes (BOOTSJ, SFINCS, NEOTRANSP) for case I at $t = 19.6$ s.

The bootstrap current calculated by BOOTSJ is smaller than the experimentally observed bootstrap current by about 49% and 69% for cases I and II, respectively. This indicates that the collisionalities reached during these discharges are too large for the collisionless approximation to be appropriate. Finite-collisionality models have previously predicted bootstrap currents in W7-X that are larger than those derived in the collisionless limit [10]. The bootstrap current densities for case I at $t = 19.6$ s predicted by BOOTSJ, NEOTRANSP, and SFINCS are compared in figure 10. The estimates of NEOTRANSP and SFINCS for this scenario agree with each

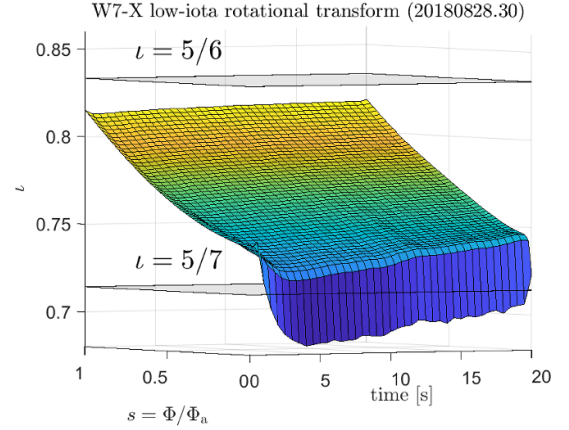


Figure 11. Evolution of the rotational transform for case I.

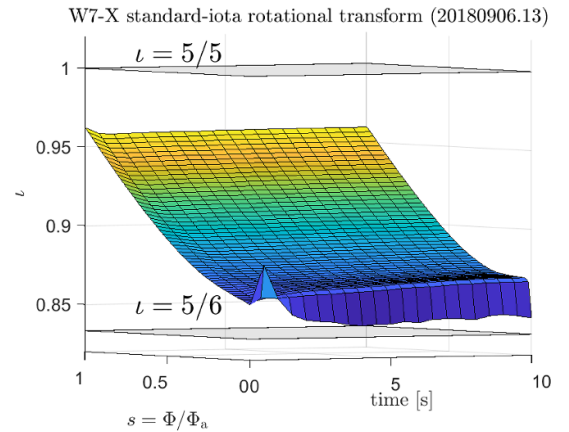


Figure 12. Evolution of the rotational transform for case II.

other and disagree with BOOTSJ. However, the NEOTRANSP and SFINCS current densities correspond to a total toroidal current of about 22 kA, which exceeds the experimental I_∞ by 35%. This highlights the point that even more detailed numerical models may be inaccurate, and validation of such models is still necessary.

The evolution of the rotational transform for case I and case II is shown in figures 11 and 12, respectively. In both cases, the rotational transform experiences an initial strong negative core shear followed by a strong positive core shear later in time. This core shear is a result of the highly-localized bootstrap current density modifying the magnetic field structure in the plasma core. Away from the plasma core, the rotational

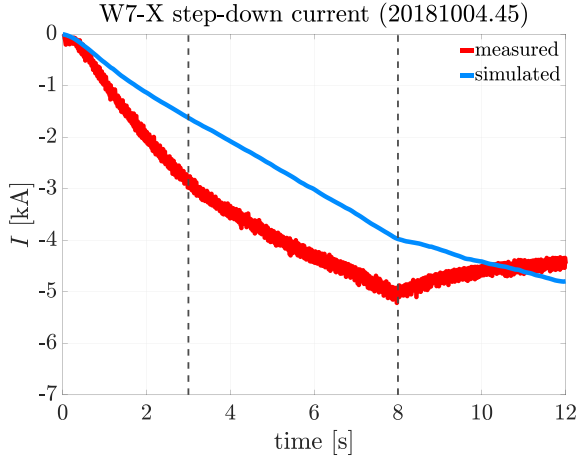


Figure 13. Comparison of simulated and measured currents for case III.

transform is weakly increased, with this effect diminishing in strength further away from the core.

In case I, THRIFT predicts that the rotational transform eventually crosses the $5/7$ rational in the core, potentially resulting in the formation of magnetic islands. The size of these islands has not been estimated, but the large shear in the rotational transform at the crossing point is expected to limit their effect on the evolution of the toroidal current. No important rational values are crossed by the rotational transform in Case II due to the smaller bootstrap current and the larger spacing between rationals. For both cases, the rotational transform is anticipated to be affected more strongly if the bootstrap current used by THRIFT better agreed with the bootstrap current seen in experiment.

3.1.2. Heating step-down. Figure 13 shows the evolution of the total toroidal current in experiment and as calculated by THRIFT for case III. No estimate of the L/R -time is made. As seen in cases I and II, the THRIFT total toroidal current is smaller than the experimentally observed toroidal current prior to the heating step-down. Both currents evolve asymptotically until $t = 3$ s. Between $t = 3$ s and $t = 8$ s, the time-derivative of the experimental current decreases, whereas the time-derivative of the THRIFT total toroidal current increases.

Considering the L/R model, the change of behavior of the experimental current can be explained by a decrease in I_∞ , an increase in $\tau_{L/R}$, or both. Since the temperature decreases and the density increases, the resistivity increased and $\tau_{L/R}$ must have decreased. Therefore, I_∞ must have decreased in this experiment through the mechanism of a decrease in the bootstrap current. No such decrease in the BOOTSJ bootstrap current or its components, shown in figure 14, is observed. To the contrary, a small increase in the BOOTSJ bootstrap current is visible just before the heating step-down, causing the time-derivative of the THRIFT total toroidal current to increase between $t = 3$ s and $t = 6$ s.

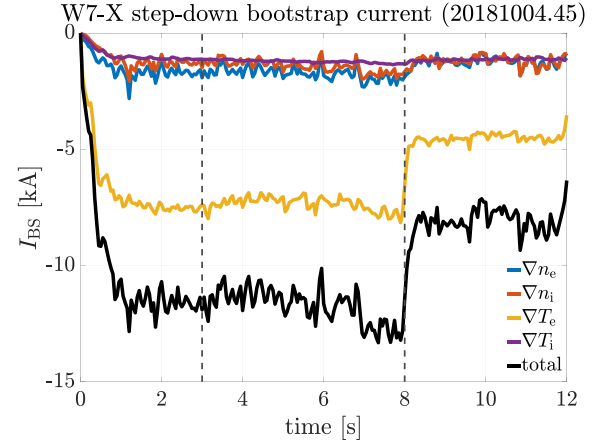


Figure 14. Breakdown of the bootstrap current for case III.

Figure 14 shows that the ∇T -driven component of the bootstrap current sharply decreases after the heating power step-down. In experiment, the direction of the evolution of the total toroidal current reverses after the heating step, indicating that the magnitude of the bootstrap current is smaller than the total toroidal current at this moment. In the simulation, the rate of change of the total current is only reduced, indicating that the bootstrap current is still larger than the total toroidal current at this moment. The THRIFT total toroidal current eventually exceeds the experimental total toroidal current, which indicates that the BOOTSJ bootstrap current is larger than the experimental bootstrap current.

Bootstrap currents for finite-collisionality W7-X plasmas that are larger or smaller than bootstrap currents in the collisionless limit are both possible. As demonstrated in figure 26 in [10], there exists a range of collisionalities for which the bootstrap current is greater than the bootstrap current in the collisionless limit. After the heating step in case III, the temperature decreases and the collisionality is expected to increase. The plasma then likely has a large enough collisionality for it to operate in this range after the heating step. These results are further indicative of BOOTSJ not being appropriate for application to W7-X, but the results also show that the toroidal current evolution calculated by THRIFT indeed responds to changes in bootstrap current and resistivity as expected.

Lastly, the evolution of the rotational transform for case III is shown in figure 15. The behavior of the rotational transform for this case prior to the heating step is similar to that seen in case I. The rotational transform also crossing the $5/7$ rational in the core in case III for the same reasons. Immediately following the heating step, a rapid increase in the rotational transform can be seen. This occurs while the time-derivative of the total toroidal current decreases. The change in rotational transform must therefore be due to the change in the source current density profile. The evolution of the rotational transform for all three cases suggests that the toroidal current distribution is of importance for investigating plasma stability, as crossing low-order rationals in the plasma is possible without (or with only small) enclosed toroidal currents.

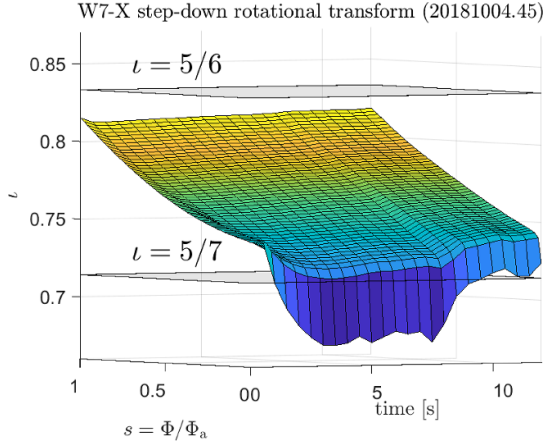


Figure 15. Evolution of the rotational transform for case III.

3.2. Current drive scenarios

A net toroidal current is necessary at W7-X to position the edge magnetic islands and control the strike line locations on the divertor [5]. Because of the long L/R time anticipated for these scenarios (~ 30 s) the total toroidal current will not quickly reach steady-state, leading to non-optimal divertor performance for significant durations. This time may be reduced if current drive is used to accelerate the evolution of the total toroidal current. The rate at which the total toroidal current evolves can be approximated by (again assuming stationary plasma profiles)

$$\dot{I}(t) = \frac{I_\infty}{\tau_{L/R}} \exp(-t/\tau_{L/R}). \quad (13)$$

Hence, by temporarily increasing the steady-state current $I_\infty = I_{\text{boot}} + I_{\text{ext}}$ through current drive, the total toroidal current may reach its saturated value (namely, the bootstrap current) earlier.

The main tool for current drive in W7-X is ECCD [22]. Experiments demonstrating the acceleration of toroidal currents up to and exceeding steady-state currents with ECCD have previously been performed in W7-X [3]. Application of ECCD in the plasma core has however also been associated with sawtooth-like behavior in W7-X [38–40]. NBCD is also a possible source of current drive at W7-X and has previously been investigated [41, 42]. In this section, the effect of ECCD on the evolution of the total current and rotational transform is considered.

The simulation for Case I was repeated and extended to $t = 50$ s. Density and temperature profiles were held constant between $t = 19.6$ s and $t = 50$ s. BOOTSJ mode and damping settings were left unchanged, but the overall bootstrap current density profile was scaled by a constant factor to obtain better agreement between the mean bootstrap current and the steady-state toroidal current estimated from experimental data. ECCD

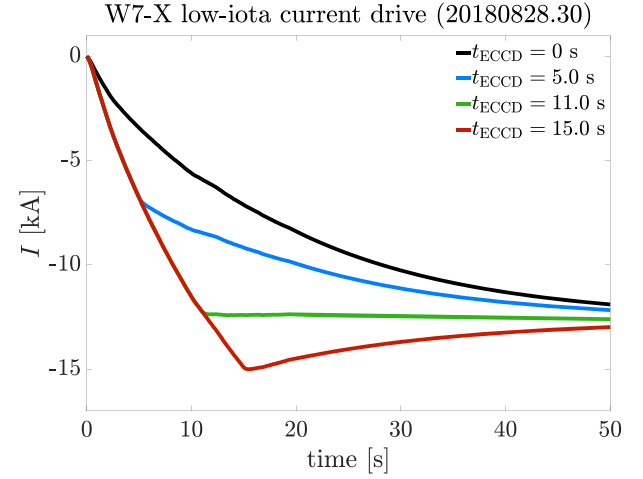


Figure 16. Evolution of the total toroidal current for the ECCD-assisted cases and unassisted case.

was mimicked using a simple Gaussian expression given by

$$J_{\text{ECCD}}(\rho) = I_{\text{norm}} \exp\left(-\frac{(\rho - r_c)^2}{w^2}\right), \quad (14)$$

$$I_{\text{norm}} = \frac{I_{\text{ECCD}}}{2\pi a^2 \tilde{I}}, \quad (15)$$

$$\tilde{I} = \frac{w}{2} \left[\sqrt{\pi} r_c \left(\text{erf}\left(\frac{1-r_c}{w}\right) + \text{erf}\left(\frac{r_c}{w}\right) \right) + w \left(\exp\left(-\frac{r_c^2}{w^2}\right) - \exp\left(-\frac{(r_c-1)^2}{w^2}\right) \right) \right], \quad (16)$$

where

r_c = deposition location in ρ -space,

w = ECCD width,

I_{ECCD} = requested amount of ECCD,

and erf is the error function. $r_c = 0.3$ and $w = 0.175$ were chosen to match the ECCD deposition pattern seen in [22]. A total ECCD current of $I_{\text{ECCD}} = 20$ kA was driven for different durations t_{ECCD} after which it was disabled and the current was allowed to freely evolve.

The evolution of the total toroidal current for different durations of ECCD is shown in figure 16. For each current drive scenario, the trend in the data suddenly changes after ECCD is disabled. If ECCD is disabled early ($t_{\text{ECCD}} = 5$ s), the total toroidal current evolves at a reduced rate towards the steady-state value of 12.6 kA. Conversely, if ECCD is disabled too late ($t_{\text{ECCD}} = 15$ s), the total toroidal current overshoots the steady-state value and it will decrease in magnitude over time. If ECCD is applied for $t_{\text{ECCD}} = 11$ s, the total toroidal current varies only little after ECCD is disabled, indicating that it has reached its steady-state value. In comparison, the total toroidal current in the unassisted case still has not saturated at $t = 50$ s.

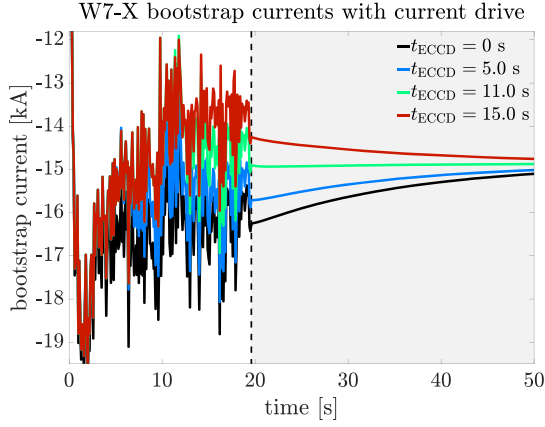


Figure 17. Evolution of the bootstrap current for the ECCD-assisted cases and unassisted case.

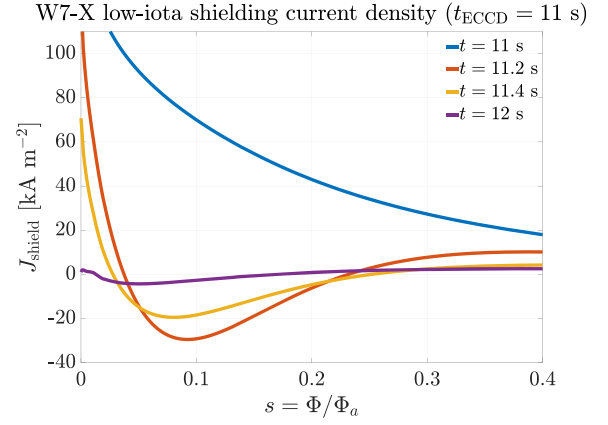


Figure 19. Evolution of the shielding current density for $t_{\text{ECCD}} = 11$ s after ECCD is deactivated.

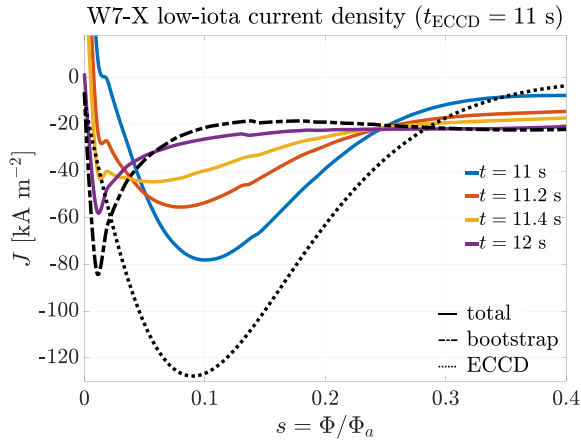


Figure 18. Evolution of the total toroidal current density for $t_{\text{ECCD}} = 11$ s after ECCD is deactivated.

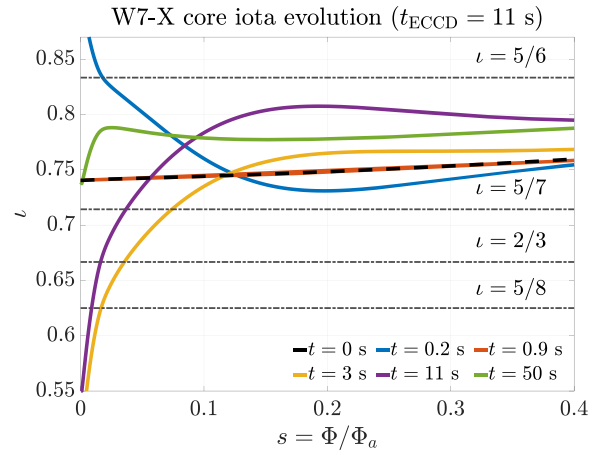


Figure 20. Evolution of the rotational transform profile for $t_{\text{ECCD}} = 11$ s after ECCD is deactivated.

Figure 17 shows the evolution of the bootstrap current for the ECCD-assisted and unassisted case. The magnitude of the bootstrap current is decreased in the ECCD-assisted cases compared to the unassisted case. This difference grows with about 0.2 kA per second while ECCD is enabled and slowly disappears after ECCD is disabled. The differences seen here would be larger by a few kA if the vacuum magnetic field was used for bootstrap calculations instead of the self-consistent magnetic field. This emphasizes the necessity of self-consistently calculating the bootstrap current, especially for devices where the bootstrap current is expected to play an important role in operation.

Figure 18 depicts the total current density in the $t_{\text{ECCD}} = 11$ s case after ECCD is disabled. Immediately preceding the ECCD shut-down, the total current density peaks at the ECCD deposition location ($s_{\text{peak}} = r_c^2 = 0.09$). After ECCD is disabled, the total current density profile will evolve in a manner to match the bootstrap current density profile. Since $I \approx I_\infty$ at this moment, the excess of total current density at s_{peak} is redistributed to regions where $J < J_{\text{boot}}$. This redistribution is explained by the evolution of the shielding current density,

shown in figure 19. At $t = 11$ s, the shielding current density is positive everywhere and peaked in the plasma core. After the ECCD is disabled the shielding current density becomes locally negative, i.e. parallel to the total current density. This ‘excess’, negative shielding current density then rapidly diffuses to regions of positive shielding current density, leading to a rapid decrease of the magnitude of the shielding current density everywhere in the plasma. These simulations also feature the aforementioned problem with the (edge) parallel electric field and the shielding current density does not completely vanish in steady-state.

The rotational transform for the case $t_{\text{ECCD}} = 11$ s is shown in figure 20. ι briefly crosses the 5/6 resonance in the plasma core when ECCD is applied. From $t = 1$ s until t_{ECCD} , the rotational transform crosses the 5/8, 2/3, and 5/7 resonances in quick succession. These crossings are closest together at $t = 11$ s, at which point their physical separations are 1.9 cm (5/8 and 2/3) and 3.4 cm (2/3 and 5/7), respectively. No explicit calculation of the width of these islands was performed but if they overlapped it could result in a loss of plasma confinement. The edge rotational transform (figure 21) initially

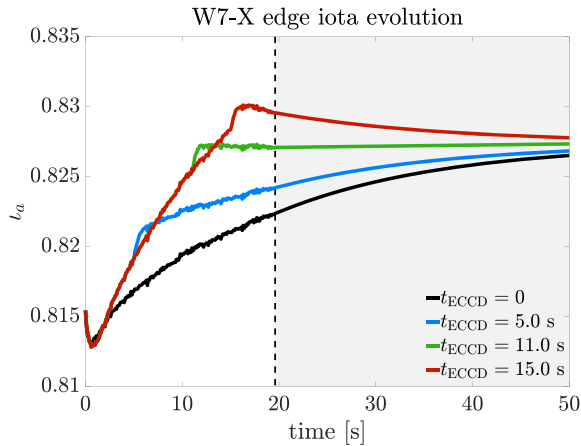


Figure 21. Evolution of the edge rotational transform for the ECCD-assisted cases and unassisted case.

decreases at the start of the simulation, attributed to an initial change in the susceptance matrix elements. Afterwards, ι_a evolves at a faster rate for the ECCD-assisted case than for the unassisted case, which is attributed to the larger rate of change of the total toroidal current in the ECCD-assisted cases. Finally, the edge rotational transform jumps when ECCD is disabled due to a change in the edge S_{12} , exemplifying how the distribution of the currents has an effect on the magnetic configuration. Noticeably, ι_a jumps to its steady-state value for $t_{\text{ECCD}} = 11$ s.

4. Discussion

In this work, the temporal evolution of net toroidal plasma currents in 3D systems was investigated. A novel implementation of the THRIFT code was performed for this purpose, which was verified using an ideal tokamak scenario. BOOTSJ was used to calculate bootstrap currents and bootstrap current densities for various W7-X scenarios. Despite being a rapid code, BOOTSJ fails to accurately calculate the bootstrap current density in the cases considered, disagreeing with both experiment and other models of the bootstrap current. The collisionalities in these cases were sufficiently high for the collisionless assumption of the bootstrap current to be far removed from the experimentally estimated bootstrap current. This reveals the need for a fast bootstrap current model that is accurate for higher collisionalities, as future reactors will not always operate in regimes of low collisionality. THRIFT was further used to consider simple current drive scenarios in W7-X.

Several future research avenues are envisioned for THRIFT. Codes such as SFINCS, PENTA, or NEOTRANSF could be interfaced with THRIFT in a manner similar to how BOOTSJ had been interfaced in this work. The resulting current evolution for each of these codes may then be compared against each other and against experiment, allowing for a benchmarking of the codes. The same approach could be taken to benchmark NBCD models (e.g. ASCOT5 [43], BEAMS3D [44]) or ECCD models (e.g. TRAVIS [45]). THRIFT could also be

used to investigate current drive scenarios in other stellarators. If a subroutine for inductive current drive were incorporated into THRIFT, it may further be used to simulate currents in tokamaks or devices featuring Ohmic transformers (e.g. NCSX [46], CTH [47]).

Acknowledgments

Computations were performed on the HPC system Cobra at the Max Planck Computing and Data Facility. This work has been carried out within the framework of the EUROfusion Consortium, funded by the European Union via the Euratom Research and Training Programme (Grant Agreement No 101052200 - EUROfusion). Views and opinions expressed are however those of the author(s) only and do not necessarily reflect those of the European Union or the European Commission. Neither the European Union nor the European Commission can be held responsible for them.

ORCID iDs

L. van Ham <https://orcid.org/0009-0002-6815-0200>
 S.A. Lazerson <https://orcid.org/0000-0001-8002-0121>
 J.C. Schmitt <https://orcid.org/0000-0002-9407-7636>
 B.F. Lee <https://orcid.org/0000-0002-3606-8467>
 M. Beurskens <https://orcid.org/0000-0002-3354-0279>
 K.J. Brunner <https://orcid.org/0000-0002-0974-0457>
 N. Chaudhary <https://orcid.org/0000-0001-5075-2487>
 J. Geiger <https://orcid.org/0000-0003-4268-7480>
 A. Langenberg <https://orcid.org/0000-0002-2107-5488>
 N. Pablant <https://orcid.org/0000-0001-6617-8459>
 K. Rahbarnia <https://orcid.org/0000-0002-5550-1801>
 G. Weir <https://orcid.org/0000-0002-2370-409X>

References

- [1] Grieger G. et al 1992 Physics optimization of stellarators *Phys. Fluids B* **4** 2081–91
- [2] Dinklage A. et al 2018 Magnetic configuration effects on the Wendelstein 7-X stellarator *Nat. Phys.* **14** 855–60
- [3] Endler M. et al 2021 Wendelstein 7-X on the path to long-pulse high-performance operation *Fusion Eng. Des.* **167** 112381
- [4] Feng Y., Sardei F., Grigull P., McCormick K., Kisslinger J. and Reiter D. 2006 Physics of island divertors as highlighted by the example of W7-AS *Nucl. Fusion* **46** 807
- [5] Gao Y. et al 2019 Effects of toroidal plasma current on divertor power depositions on Wendelstein 7-X *Nucl. Fusion* **59** 106015
- [6] Gao Y., Jakubowski M.W., Drewelow P., Pisano F., Puig Sitjes A., Niemann H., Ali A. and Cannas B. 2019 Methods for quantitative study of divertor heat loads on W7-X *Nucl. Fusion* **59** 066007
- [7] Strand P.I. and Houlberg W.A. 2001 Magnetic flux evolution in highly shaped plasmas *Phys. Plasmas* **8** 2782–892
- [8] Wolf R.C. et al 2019 Performance of Wendelstein 7-X stellarator plasmas during the first divertor operation phase *Phys. Plasmas* **26** 082504
- [9] Peeters A.G. 2000 Bootstrap current and its consequences *Plasma Phys. Control. Fusion* **42** B231

- [10] Beidler C.D. *et al* 2011 Benchmarking of the mono-energetic transport coefficients - results from the International Collaboration on Neoclassical Transport in Stellarators (ICNTS) *Nucl. Fusion* **51** 076001
- [11] Geiger J., Beidler C.D., Drevlak M., Maaßberg H., Nührenberg C., Suzuki Y. and Turkin Y. 2010 Effects of net currents on the magnetic configuration of W7-X *Contrib. Plasma Phys.* **50** 770–4
- [12] Landreman M., Smith H.M., Mollén A. and Helander P. 2014 Comparison of particle trajectories and collision operators for collisional transport in nonaxisymmetric plasmas *Phys. Plasmas* **21** 042503
- [13] Hirshman S.P., Shaing K.C., van Rij W.I., Beasley C.O. and Crume E.C. 1986 Plasma transport coefficients for nonsymmetric toroidal confinement systems *Phys. Fluids* **29** 2951–9
- [14] Van Rij W.I. and Hirshman S.P. 1989 Variational bounds for transport coefficients in three-dimensional toroidal plasmas *Phys. Fluids B* **1** 563–9
- [15] Turkin Y., Beidler C.D., Maaberg H., Murakami S., Tribaldos V. and Wakasa A. 2011 Neoclassical transport simulations for stellarators *Phys. Plasmas* **18** 022505
- [16] Maaßberg H., Beidler C.D. and Turkin Y. 2009 Momentum correction techniques for neoclassical transport in stellarators *Phys. Plasmas* **16** 072504
- [17] Hakan S. 2022 *private communication*
- [18] Shaing K.C., Hirshman S.P. and Tolliver J.S. 1986 Parallel viscosity-driven neoclassical fluxes in the banana regime in nonsymmetric toroidal plasmas *Phys. Fluids* **29** 2548–55
- [19] Shaing K.C., Crume E.C., Tolliver J.S., Hirshman S.P. and Van Rij W.I. 1989 Bootstrap current and parallel viscosity in the low collisionality regime in toroidal plasmas *Phys. Fluids B* **1** 148–52
- [20] Shaing K.C., Carreras B.A., Dominguez N., Lynch V.E. and Tolliver J.S. 1989 Bootstrap current control in stellarators *Phys. Fluids B* **1** 1663–70
- [21] Dinklage A. *et al* 2021 Validation of theory-based models for the control of plasma currents in W7-X divertor plasmas *Nucl. Fusion* **61** 126022
- [22] Yu Turkin Y., Maassberg H., Beidler C.D., Geiger J. and Marushchenko N.B. 2006 Current control by ECCD for W7-X *Fusion Sci. Technol.* **50** 387–94
- [23] Neuner U. *et al* 2021 Measurements of the parameter dependencies of the bootstrap current in the W7-X stellarator *Nucl. Fusion* **61** 036024
- [24] Strand P.I. and Houlberg W.A. 2001 Solution techniques for magnetic flux evolution in toroidal plasmas *Fusion Technol.* **39** 1091–5
- [25] Hirshman S.P. and Whitson J.C. 1983 Steepest-descent moment method for three-dimensional magnetohydrodynamic equilibria *Phys. Fluids* **26** 3553–68
- [26] Lazerson S., Schmitt J., Zhu C., Breslau J., All STELLOPT Developers and USDOE Office of Science 2020 STELLOPT (<https://doi.org/10.11578/dc.20180627.6>)
- [27] Kruskal M.D. and Kulsrud R.M. 1958 Equilibrium of a magnetically confined plasma in a toroid *Phys. Fluids* **1** 265–74
- [28] Schmitt J.C. 2011 3-D equilibrium reconstruction in the HSX stellarator *PhD Thesis* University of Wisconsin-Madison
- [29] Mikkelsen D.R. 1989 Current relaxation time scales in toroidal plasmas *Phys. Fluids B* **1** 333–9
- [30] Sauter O., Angioni C. and Lin-Liu Y.R. 1999 Neoclassical conductivity and bootstrap current formulas for general axisymmetric equilibria and arbitrary collisionality regime *Phys. Plasmas* **6** 2834–9
- [31] Wesson J.A. 2004 *Tokamaks* 3rd edn (Clarendon)
- [32] Ware A.S., Spong D.A., Berry L.A., Hirshman S.P. and Lyon J.F. 2006 Bootstrap current in quasi-symmetric stellarators *Fusion Sci. Technol.* **50** 236–44
- [33] Schmitt J.C., Probert P., Anderson D. and Talmadge J.N. 2007 Measurement of the Pfirsch-Schlüter and bootstrap currents in HSX *17th Int. Toki Conf. and 16th Int. Stellarator/Heliotron Workshop 2007 (ITC/ISHW2007)*
- [34] Raghunathan M., Graves J.P., Cooper W.A., Pedro M. and Sauter O. 2016 Simulation of bootstrap current in 2D and 3D ideal magnetic fields in tokamaks *Nucl. Fusion* **56** 092004
- [35] Landreman M., Buller S. and Drevlak M. 2022 Optimization of quasi-symmetric stellarators with self-consistent bootstrap current and energetic particle confinement *Phys. Plasmas* **29** 082501
- [36] Escoto F.J., Velasco J.L., Calvo I., Landreman M. and Parra F.I. 2024 MONKES: a fast neoclassical code for the evaluation of monoenergetic transport coefficients in stellarator plasmas *Nucl. Fusion* **64** 076030
- [37] Lazerson S.A. *et al* 2020 Validation of the BEAMS3D neutral beam deposition model on Wendelstein 7-X *Nucl. Fusion* **60** 076020
- [38] Wolf R.C. *et al* 2019 Electron-cyclotron-resonance heating in Wendelstein 7-X: a versatile heating and current-drive method and a tool for in-depth physics studies *Plasma Phys. Control. Fusion* **61** 014037
- [39] Zanini M. *et al* 2020 ECCD-induced sawtooth crashes at W7-X *Nucl. Fusion* **60** 106021
- [40] Zocco A. *et al* 2021 W7-X and the sawtooth instability: towards realistic simulations of current-driven magnetic reconnection *Nucl. Fusion* **61** 086001
- [41] Lazerson S.A. *et al* 2021 First neutral beam experiments on Wendelstein 7-X *Nucl. Fusion* **61** 096008
- [42] Lazerson S.A. *et al* 2021 Modeling and measurement of energetic particle slowing down in Wendelstein 7-X *Nucl. Fusion* **61** 096005
- [43] Hirvijoki E., Asunta O., Koskela T., Kurki-Suonio T., Miettunen J., Sipilä S., Snicker A. and Äkäslompolo S. 2014 ASCOT: solving the kinetic equation of minority particle species in tokamak plasmas *Comput. Phys. Commun.* **185** 1310–21
- [44] McMillan M. and Lazerson S.A. 2014 BEAMS3D neutral beam injection model *Plasma Phys. Control. Fusion* **56** 095019
- [45] Marushchenko N.B., Turkin Y. and Maassberg H. 2014 Ray-tracing code TRAVIS for ECR heating, EC current drive and ECE diagnostic *Comput. Phys. Commun.* **185** 165–76
- [46] Nelson B.E. *et al* 2003 Design of the national compact stellarator experiment (NCSX) *Fusion Eng. Des.* **66–68** 169–74
- [47] Hartwell G.J., Knowlton S.F., Hanson J.D., Ennis D.A. and Maurer D.A. 2017 Design, construction and operation of the compact toroidal hybrid *Fusion Sci. Technol.* **72** 76–90